Characteristic length scales of the electrically induced insulator-to-metal transition

Theodor Luibrand,[1,*] Adrien Bercher,[2,*] Rodolfo Rocco,[3,*] Farnaz Tahouni-Bonab,[1] Lucia Varbaro,[2] Carl Willem Rischau,[2] Claribel Domínguez,[2] Yixi Zhou,[2] Weiwei Luo,[2] Soumen Bag,[3] Lorenzo Fratino,[3,4] Reinhold Kleiner,[1] Stefano Gariglio,[2] Dieter Koelle,[1] Jean-Marc Triscone,[2] Marcelo J. Rozenberg,[3] Alexey B. Kuzmenko,[2] Stefan Guénon,[1] and Javier del Valle[2,5,†]

[1]Physikalisches Institut, Center for Quantum Science (CQ) and LISA+, Eberhard Karls Universität Tübingen, Auf der Morgenstelle 14, Tübingen 72076, Germany

[2]Department of Quantum Matter Physics, University of Geneva, 24 Quai Ernest-Ansermet, 1211 Geneva, Switzerland

[3]Université Paris-Saclay, CNRS Laboratoire de Physique des Solides, 91405, Orsay, France

[4]Laboratoire de Physique Théorique et Modélisation, CNRS UMR 8089, CY Cergy Paris Université, 95302 Cergy-Pontoise Cedex, France

[5]Department of Physics, University of Oviedo, C/ Federico García Lorca 18, 33007 Oviedo, Spain

(Received 1 November 2022; accepted 20 January 2023; published 13 February 2023)

Some correlated materials display an insulator-to-metal transition as the temperature is increased. In most cases, this transition can also be induced electrically, resulting in volatile resistive switching due to the formation of a conducting filament. While this phenomenon has attracted much attention due to potential applications, many fundamental questions remain unaddressed. One of them is its characteristic lengths: What sets the size of these filaments, and how does this impact resistive switching properties? Here, we use a combination of wide-field and scattering-type scanning near-field optical microscopies to characterize filament formation in $NdNiO_3$ and $SmNiO_3$ thin films. We find a clear trend: Smaller filaments increase the current density, yielding sharper switching and a larger resistive drop. With the aid of numerical simulations, we discuss the parameters controlling the filament width and, hence, the switching properties.

DOI: 10.1103/PhysRevResearch.5.013108

I. INTRODUCTION

Many correlated materials, such as the vanadate and rare-earth nickelate families, are well-known for their insulator-to-metal transition (IMT) [1–3]. The transition into the metallic state can be induced by increasing temperature, adding dopants, or applying high pressures [4–6], but it can also be triggered electrically [7–12]. A large enough applied voltage or current can create a percolative metallic filament due to Joule heating [13], drastically reducing the resistance of the system [14–20]. We must note that this filament is not caused by the diffusion of ions under strong electric fields, as commonly observed in resistive random access memories [21], but rather by a local phase transition from insulator to metal. When the voltage (current) is removed, the filament disappears, resulting in volatile resistive switching [22]. This phenomenon has attracted a lot of attention due to promising applications in emerging technologies, such as emulating neuronal spiking for neuromorphic computing [23–29], probabilistic bits for stochastic computing [30–32], or serving as electro-optical switches for optoelectronics [33–37]. Despite this, many fundamental aspects of the electrically induced IMT are poorly understood. One of the most salient issues is the typical length scale of this process: What sets the size of the metallic filaments or the number of them? Similarly, how do these characteristic lengths affect the resistive switching properties, i.e., the sharpness of the switch ($\partial V/\partial I$) or the total resistive drop? Understanding this is not only of fundamental interest but also key for designing device applications.

Here, we use a combination of wide-field optical microscopy [38] and scattering-type scanning near-field optical microscopy (s-SNOM) [39] to characterize filament length scales during the electrically induced IMT in $NdNiO_3$ and $SmNiO_3$ microdevices. These compounds are two well-known members of the rare-earth nickelate family [2,6]. They both display an IMT concomitant with a structural phase transition, but there are rather important differences between the two. $NdNiO_3$ has a sharp IMT $\sim$120 K (depending on epitaxial strain) with a resistivity drop of more than two orders of magnitude [Fig. 1(a)]. $SmNiO_3$ on the other hand, displays a smooth IMT $\sim$400 K, with an order of magnitude resistivity change [2,6]. Such different IMTs allow us to contrast the results from both materials and to determine which parameters govern filament length scales.

II. METHODS

We fabricated two-terminal microdevices on top of our $NdNiO_3$ and $SmNiO_3$ films, as depicted in Fig. 1(b). The nickelate films ($\sim$40 nm thick, Fig. 6 in the Supplemental Material [40]) were grown on $LaAlO_3$ (001) substrates

*These authors contributed equally to this work.
†javier.delvalle@uniovi.es

Published by the American Physical Society under the terms of the Creative Commons Attribution 4.0 International license. Further distribution of this work must maintain attribution to the author(s) and the published article's title, journal citation, and DOI.

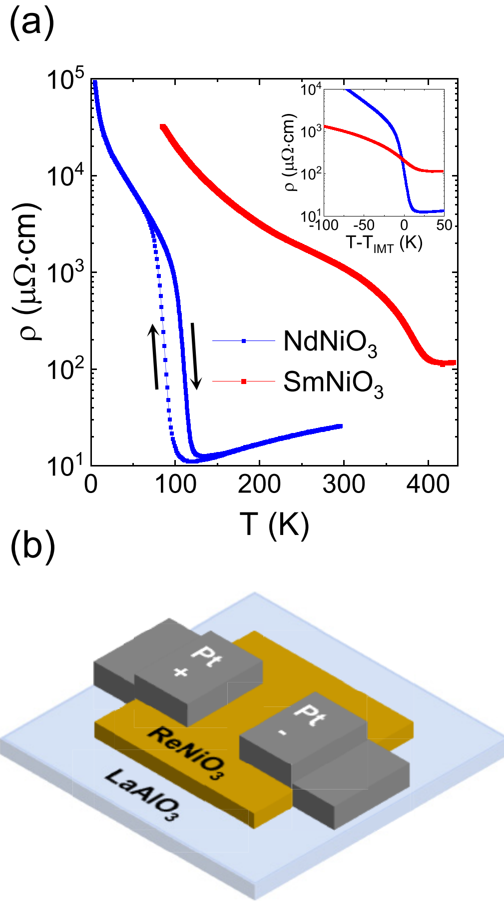

FIG. 1. Sample characteristics. (a) Resistivity vs temperature for ~40-nm-thick $NdNiO_3$ (blue) and $SmNiO_3$ (red) thin films. Inset: Resistivity plotted as a function of T-T_{IMT}. T_{IMT} was calculated finding the maximum of $\partial \log(\rho)/\partial T$, where ρ is the resistivity. Only the warmup branch is shown. (b) Schematic representation of the two-terminal devices. Nickelate islands (brown) were patterned on top of a $LaAlO_3$ substrate (blue). Two platinum electrodes (gray) were used to electrically trigger the insulator-to-metal transition (IMT). The schematic is not at scale.

using off-axis magnetron sputtering. We used a combination of optical lithography and ion etching to define isolated 360×130 μm nickelate islands, on top of which we patterned two planar Pt electrodes using a second optical lithography and on-axis Pt sputtering (see Appendix A). The electrodes are 20 μm wide, with a 20 μm gap between them (10×10 μm for the s-SNOM experiments). The IMT can be triggered by applying a large enough voltage or current across the gap. To image this phenomenon, we take advantage of the large reflectivity change across the IMT [10]. We use optical microscopy to capture the distribution of metallic/insulating domains in the gap between electrodes [18]. We do so *in operando*, i.e., while applying a variable bias current, which allows us to capture clear images of the percolating filament (see Appendix B).

III. EXPERIMENTAL RESULTS

Figure 2(a) shows the voltage V as a function of the current I in a $NdNiO_3$ microdevice at several temperatures below the IMT temperature, i.e., the film is in the insulating state when no current is applied. As the current is ramped up, the voltage rises steeply until a threshold is reached, after which a steep voltage reduction takes place. Such a drop marks the moment when the electrically induced IMT occurs and a filament percolates between the electrodes. This is a well-known phenomenon [14–20], and it can be readily observed with our imaging setup. The filament widens when current is further increased, shrinks for decreasing current, and disappears at low enough current values (see Appendix D and the Supplemental Material [40]), in accordance with the volatile V-I curves in Fig. 2(a). We must note that some of the V-I curves feature two discontinuities. In the current range between them, the system is not stationary but rapidly oscillates between a high and a low resistance state, as further discussed in Appendix E. As expected, we find the filament width to be strongly dependent on the bias current, like what has been reported in previous works [15,16,18]. The bulk of this paper focuses on how other factors, such as temperature or material properties, also play a key role at setting filament size.

Figure 2(a) shows a clear trend: The voltage drop becomes sharper and larger as the temperature is lowered. This feature is also observed in $SmNiO_3$ microdevices [Fig. 2(d)], where resistive switching at room temperature is modest, very gradual, and without discontinuities. As the temperature is lowered, the drop becomes steeper and discontinuous. Comparing $NdNiO_3$ and $SmNiO_3$, resistive switching is sharper for the former. Figures 2(b) and 2(e) show optical microscopy images of filaments in $NdNiO_3$ and $SmNiO_3$, respectively, for the same applied current, $I = 20$ mA. Images at two different temperatures are displayed for each material, showing distinctively thinner filaments at lower temperatures in both cases. This is better appreciated in Figs. 2(c) and 2(f), where filament width (for $I = 20$ mA) is plotted as a function of temperature. Lower temperatures yield thinner filaments and, therefore, higher current densities. Moreover, comparing $NdNiO_3$ and $SmNiO_3$, we can see that filaments are much thinner in $NdNiO_3$. Therefore, for a fixed bias current, the filament size is strongly dependent on the material and the base temperature. Figure 2 as a whole establishes a strong connection between filament size and V-I characteristics: Thinner filaments (higher current densities) lead to sharper and larger resistive switching.

While optical microscopy is a versatile tool to visualize metallic/insulating areas at multiple temperatures and currents, its spatial resolution is limited by diffraction. To get more detailed images, we performed *in operando* cryogenic s-SNOM measurements in $NdNiO_3$ devices, using a setup such as the one depicted in Fig. 3(a). The spatial resolution of this atomic force microscopy (AFM)-based technique is limited only by the tip radius (~20 nm) [39], allowing us to obtain high-resolution AFM and near-field images of the filaments. Figures 3(b) and 3(c) show topography and s-SNOM images at 18 and 70 K, respectively. Images for 0, 10, and 20 mA are displayed. For similar currents, filaments are thinner at lower temperatures, in accordance with wide-field optical images in Fig. 2. Moreover, s-SNOM allows us to resolve clear qualitative differences between both temperatures. Images taken at 18 K show a single, intense filament percolating between electrodes, while at higher temperature multiple filaments appear.

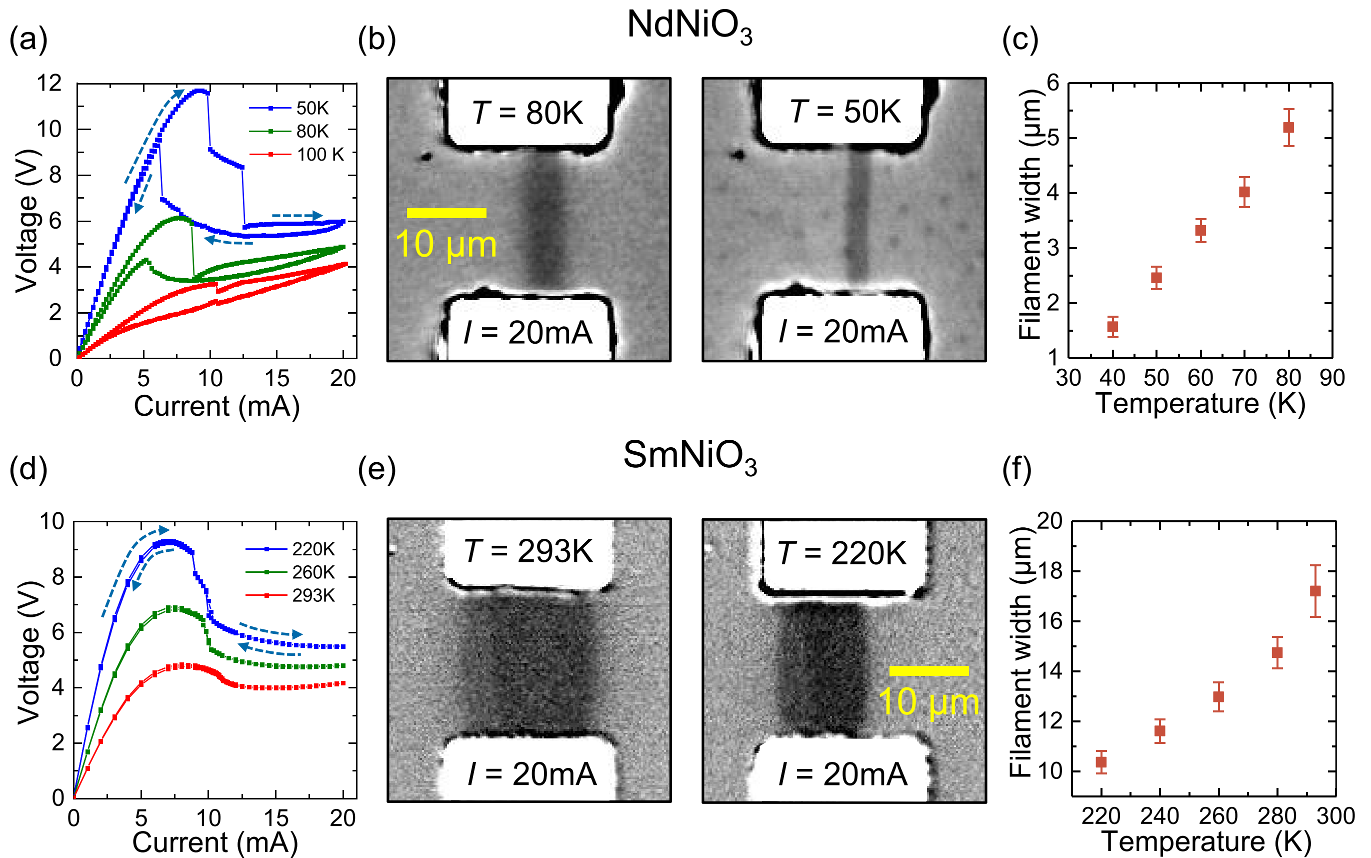

FIG. 2. Connection between resistive switching properties and filament size. (a) and (d) Voltage vs current curves for $NdNiO_3$ and $SmNiO_3$ microdevices, respectively. Several temperatures are plotted for each material. (b) and (e) Wide-field optical microscopy images of filaments in $NdNiO_3$ and $SmNiO_3$, respectively. Current is 20 mA for all four images. Two different temperatures are shown for each material. For the $NdNiO_3$ images, reflectivity was normalized using a region far from the gap. For $SmNiO_3$, differential images are shown, where at each point, the reflectivity at $I = 0$ mA is subtracted. (c) and (f) Filament width vs temperature at $I = 20$ mA. The width was determined using a Gaussian fitting of line scans perpendicular to the filament direction, taking the full width at half maximum as filament width. The error bars show the standard deviation of the distribution of widths.

Thus, lower temperatures favor a winner-takes-all situation in which a single filament carries all the current.

IV. RESISTOR NETWORK SIMULATIONS

To understand these results, we performed numerical simulations in which we model our system as a two-dimensional resistor network [Fig. 4(a)] [10,25]. Each node in the network can be either metallic or insulating, depending on the local temperature and a Landau free energy functional that mimics the IMT. The insulating state resistivity increases as the temperature is decreased, following a variable range hopping dependence [inset of Fig. 4(b)]. Currents and voltages at each node are calculated by solving Kirchhoff's laws. Local temperature is updated in each simulation time step, considering Joule heating and heat conduction. Each node of the network dissipates heat horizontally to its neighbors and vertically to the underlying substrate. We keep the substrate temperature constant, without gradients, which means we do not consider horizontal heat flow through the substrate. However, this contribution can also be captured by our model since it would effectively result in a renormalization of the lateral heat conductivity through the film. A more detailed description of the simulations can be found in Appendix C. This simple model reproduces experimental results with only a few parameters [Fig. 4(b)], allowing us to identify which ones play a key role.

Figure 4(c) shows simulated two-dimensional resistivity maps of the devices for three different values of current and base temperature. As expected, filaments are strongly dependent on the bias current. Also, like the experiments, filaments become narrower as the base temperature is lowered. The material confines current flow into a smaller region at lower temperatures. This in turn induces higher current densities, increasing local Joule heating and greatly affecting the temperature distribution across the device, as can be seen in Fig. 4(d). As the filament narrows, its inner temperature increases. Therefore, thinner filaments induce a stronger current-temperature feedback, which is a key factor controlling switching dynamics [10,19,30]. Strong feedback makes the device susceptible to runaway effects which manifest as discontinuities in the experimental V-I curves [30]. As a result, the thinner the filament and the higher its current-temperature feedback, the larger the discontinuities in the V-I curves. Experimentally, such

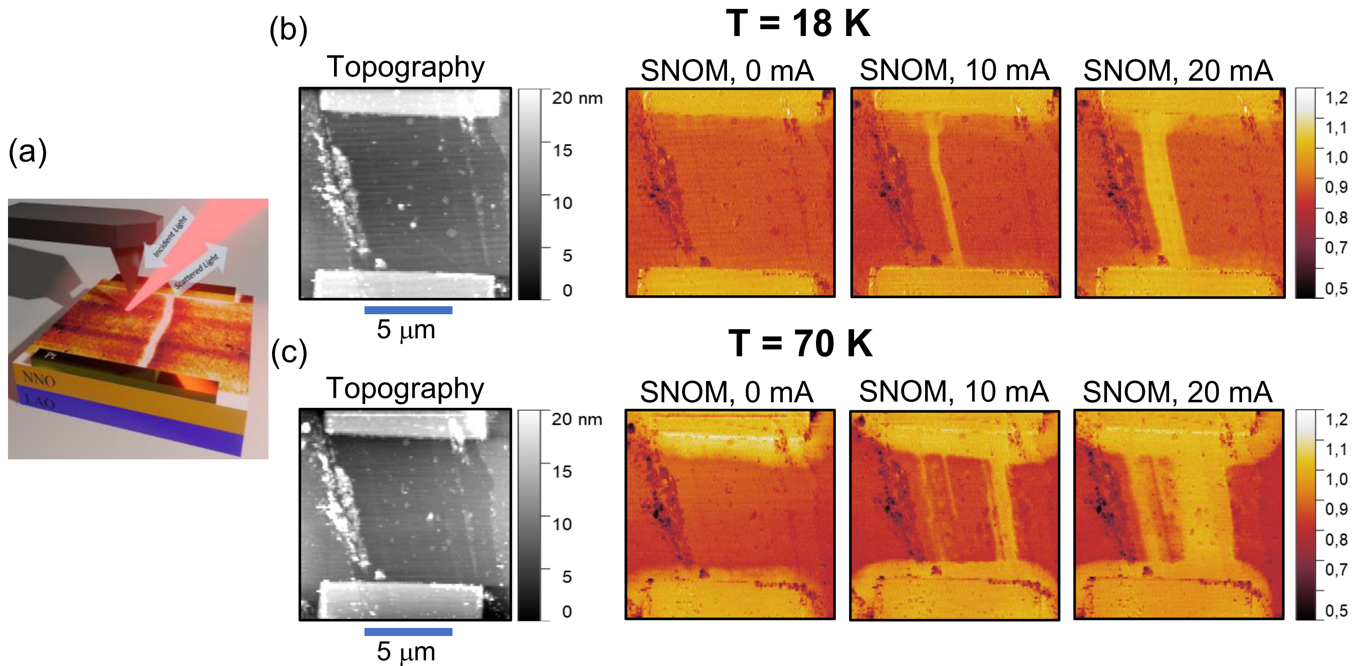

FIG. 3. High-resolution scattering-type scanning near-field optical microscopy (s-SNOM) imaging and presence of multiple percolating filaments. (a) Schematic representation of the s-SNOM setup. Infrared light (wavelength 10 μm) is focused at a metal-coated atomic force microscopy (AFM) tip, which further focuses light into an area comparable to the tip radius (∼20 nm). The tip-scattered signal is determined by the optical conductivity of the area of the material directly underneath the tip, allowing us to get high-resolution images of metallic (high signal) and insulating (low signal) domains. The AFM works in tapping mode and the s-SNOM signal is detected at the third and second harmonic to filter out the far-field component, as described in Appendix B. (b) and (c) Topography and s-SNOM amplitude images for $NdNiO_3$ microdevices at $T = 18$ and 70 K, respectively. The s-SNOM signal was normalized using the Pt electrode as reference. s-SNOM data for three different current values is shown. At 70 K, the $NdNiO_3$ surrounding the Pt electrodes exhibits an enhanced conductivity even in the absence of current, likely caused by a slight T_{IMT} depression in that area. Although we do not know for certain, this could be caused by the lithographic process or by electrode-induced strain or doping [41].

discontinuities are observed to be bigger and more frequent at lower temperatures, especially for $NdNiO_3$. These are the same conditions in which the thinnest filaments are observed.

V. DISCUSSION

Since filament size determines switching properties, it is key to identify which parameters control the ability of the material to confine current into smaller or larger areas. Here, we analyze two contributions: the resistivity difference across the IMT and the thermal conductivity of the substrate. The resistivity contrast between the insulating (ρ_{ins}) and metallic (ρ_{met}) phases is expected to play a major role since it corresponds to the resistivities outside and inside the filament. When $\rho_{ins} \gg \rho_{met}$, the current is strongly focused into the filament, reducing Joule heating outside. This keeps the insulating areas cold and confines the filament in a small region. However, as ρ_{ins} decreases, the insulator becomes leaky, allowing current flow and power dissipation outside the filament and reducing its confinement.

The temperature dependence of the resistivity implies that, as temperature increases, so does power dissipation outside the filament, increasing its width. For instance, the voltage at $I = 5$ a.u. is half as large for $T = 90$ a.u. than for $T = 18$ a.u. [Fig. 4(b)], but the insulating resistivity is ∼8 times smaller. As a result, power dissipation outside the filament is increased by a factor of 2 at $T = 90$ a.u. vs $T = 18$ a.u. These differences in resistivity explain not only the temperature dependence of the filament size but also the differences observed between $NdNiO_3$ and $SmNiO_3$. The former has a larger resistivity change across the IMT [Fig. 1(a)] [6] and is therefore expected to focus current into thinner filaments. Furthermore, the presence of single or multiple percolating filaments (Fig. 3) can be understood in a similar light. For $\rho_{ins} \gg \rho_{met}$, the current will crowd through the first hotspot that metallizes, favoring a winner-takes-all scenario.

However, the resistivity drop across the IMT is not the only mechanism that can explain the differences in filament size. Thermal properties are also expected to play a crucial role, and they can provide a similarly satisfactory explanation. The thermal conductivity of $LaAlO_3$ is not constant but decreases from 60–70 W/(m K) at 60 K to ∼15 W/(m K) at 300 K [42]. This means that the substrate can more efficiently evacuate heat at lower temperatures, keeping the areas surrounding the filament cold. The filament is therefore confined to a smaller region, as simulations have recently shown [19]. Therefore, thermal properties can also explain the smaller filament size at lower temperatures, as well as accounting for the overall differences between $NdNiO_3$ and $SmNiO_3$, which have IMTs in very different temperature ranges.

Unfortunately, it is difficult to disentangle the contributions due to the resistivity change across the IMT and the substrate thermal conductivity. Both parameters decrease as

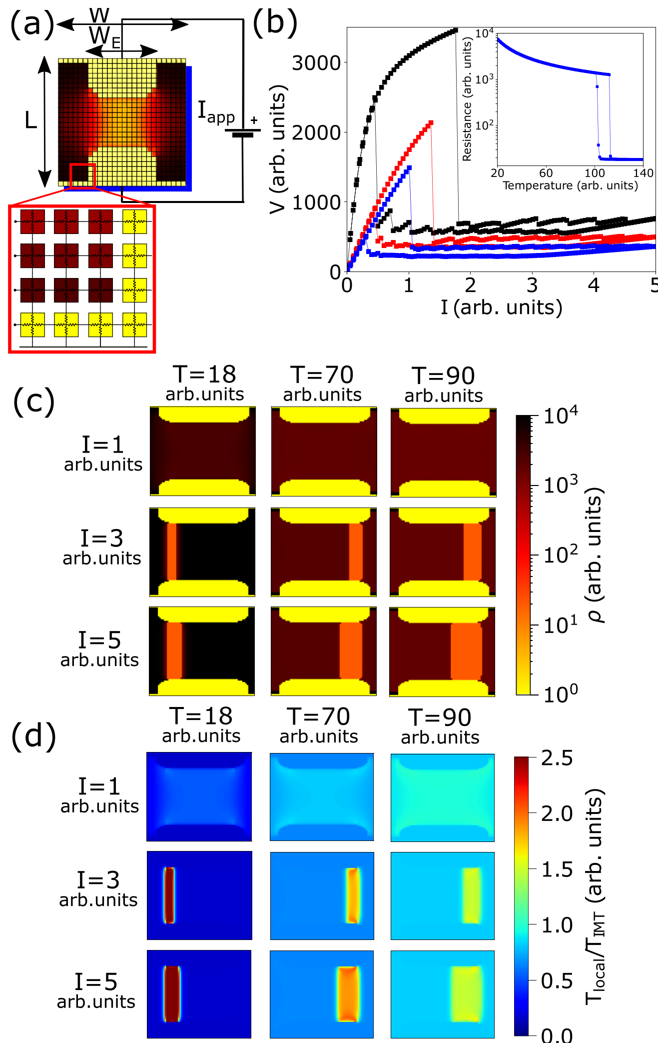

FIG. 4. Resistor network simulations and current focusing effect. (a) Schematic representation of the simulated resistor network (size $W \times L$). Low-resistance electrodes (yellow) define an oxide gap where individual nodes could be either metallic (orange) or insulating (dark brown), as described in Appendix C. (b) Simulated voltage vs current curves for three different temperatures: 18 a.u. (black), 70 a.u. (red), and 90 a.u. (blue). Inset: Simulated resistance vs temperature of the device. (c) Simulated, two-dimensional resistivity plots for all combinations of three currents (1, 3, and 5 a.u.) and three device base temperatures (18, 70, and 90 a.u.). Resistivity is plotted in logarithmic color scale. (d) Simulated, two-dimensional temperature plots for all combinations of three currents (1, 3, and 5 a.u.) and three device base temperatures (18, 70, and 90 a.u.). Temperature is plotted in linear color scale and normalized to the transition temperature (120 a.u.).

temperature is increased. Within the nickelate family, it is observed that, as the transition temperature increases (with the reduction of the rare-earth ion radius), the resistivity drop across the IMT decreases [2,6]. A similar trend is observed in the V_2O_3, VO_2, and V_3O_5 family [10]. Therefore, it is not feasible to compare a material featuring a high-temperature IMT with a large resistivity change with another system having a low-temperature IMT with a small resistivity change.

A way to overcome this drawback is to compare, for the same material, samples with different IMT quality. We fabricated two $NdNiO_3$ films: one with a high-quality IMT and a second one subjected to a 120 °C, 30 min annealing in vacuum. The annealing creates oxygen vacancies, reducing the resistivity change across the IMT, as seen in Fig. 5(a). This has clear consequences in the resistive switching properties, which are smoother for the annealed sample [Fig. 5(b)]. Furthermore, there are notable differences in the filament, as can be seen in Figs. 5(c) and 5(d). The annealed device shows much less contrast and homogeneity within the metallic area, perhaps due to the formation of multiple filaments. This differs from the well-defined, intense filament for the nonannealed sample and points to less metallization and current focusing. This confirms that the resistivity change across the IMT is a key parameter controlling resistive switching and filament characteristics, although it does not rule out important contributions from thermal conductivity.

VI. CONCLUSIONS

In summary, we have used a combination of *in operando* standard and scanning near-field optical microscopies to study the characteristic lengths of filament formation during the electrically induced IMT. We found that, in addition to bias current, filament width is strongly dependent on base temperature and the specific material. Lower setup temperatures yield thinner filaments, increasing current density and local temperature, leading to sharper resistive switching properties. With the aid of resistor network simulations, we discussed the material properties that control filament size, underlining the importance of the resistivity drop across the IMT as well as the thermal conductivity of the substrate.

Our results support recent works concerning another fundamental aspect of the electrically induced IMT: switching dynamics [10,11]. It was proposed that a large resistivity ratio between insulator and metal would induce higher current focusing, increasing local Joule heating within the filament and explaining the different switching timescales observed in V_2O_3, VO_2, V_3O_5, $NdNiO_3$, and $SmNiO_3$. However, direct evidence of this has been lacking so far. In this paper, we provide a systematic study of the characteristic length scales of the electrically induced IMT, unveiling a strong connection between resistivity, thermal properties, filament size, and resistive switching characteristics. The mechanisms outlined here are simple and general and could be applicable to other types of resistive switching, such as ReRAM. Considered together with recent developments in the field [10,11,22], it completes a simple and unified picture of the length and time scales of filament nucleation, growth and relaxation, as well as underlining their importance for developing technologies based on the IMT.

ACKNOWLEDGMENTS

The authors thank Marco Lopes for his support during the fabrication and measurement of these samples. The sample fabrication and project coordination were funded by the Swiss National Science Foundation through an Ambizione Fellowship (No. PZ00P2_185848). The oxide growth was supported by the European Research Council under the European Union's Seventh Framework Program (No.

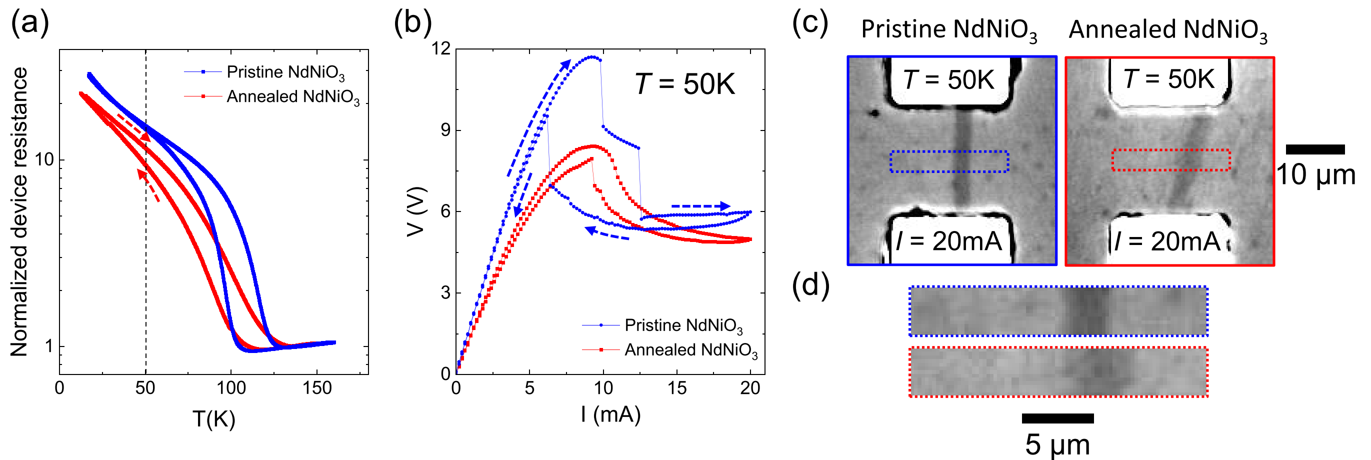

FIG. 5. Resistive switching and filament characteristic in pristine and annealed $NdNiO_3$. (a) Two-probe device resistance vs temperature on pristine (blue) and annealed (red) $NdNiO_3$ films. (b) Voltage vs current at $T = 50$ K for a pristine (blue) and annealed (red) sample. (c) Wide-field microscopy image of filament formation in pristine (left) and annealed (right) $NdNiO_3$. $T = 50$ K and $I = 20$ mA in both cases. Reflectivity was normalized using an area far from the gap region. (d) Zoomed image into the central part of the filament for pristine (top) and annealed (bottom) $NdNiO_3$. $T = 50$ K and $I = 20$ mA in both cases.

FP7/2007-2013)/ERC Grant Agreement No. 319286 Q-MAC and the Swiss National Science Foundation Project No. 200020-179155. W.R. was supported by the U.S. Office of Naval Research through the NICOP Grant No. N62909-21-1-2028. s-SNOM measurements were supported by the Swiss National Science Foundation through a Research Grant No. 200020_201096. Simulations were funded by the French ANR project "MoMA" ANR-19-CE30-0020. T.L. acknowledges support by the Cusanuswerk, Bischöfliche Studienförderung. J.d.V. acknowledges support from the Spanish Ministry of Science through a Ramón y Cajal Fellowship (No. RYC2021-030952-I) and from Asturias FICYT under Grant No. AYUD/2021/51185 with the support of FEDER funds.

APPENDIX A: DEVICE AND THIN FILM STRUCTURE AND FABRICATION

We grew $NdNiO_3$ and $SmNiO_3$ oxide films on (001)-oriented $LaAlO_3$ substrates using off-axis magnetron sputtering in an $Ar:O_2$ (3.5:1) mixture at a pressure of 180 mTorr and substrate temperature of 460 °C. Films are ~40–45 nm thick and grow epitaxially, as can be seen using x-ray diffraction (XRD) [Figs. 6(c) and 6(d)].

For microdevice fabrication, a combination of techniques was used. First, we patterned isolated $NdNiO_3$ and $SmNiO_3$ islands using optical lithography and Ar ion beam milling. This allows us to measure each device independently since it is electrically isolated from the others. After this, we patterned Pt electrodes on top of these islands. For that, we used optical lithography followed by on-axis Pt sputtering at room temperature and a lift-off in acetone. Pt thickness is ~40 nm. and the gap size is 20×20 μm. For the s-SNOM measurements, a further lithographic step was used. Optical lithography does not create smooth electrode edges. This is very challenging for SNOM since the tip is tripped by the electrode irregularities. To improve this, we used electron beam lithography and a second Pt evaporation to define 10×10 μm electrodes with smooth edges.

APPENDIX B: MICROSCOPY TECHNIQUES

We used an optical wide-field microscope that facilitates simultaneous imaging and electrical transport measurements [38]. The device under investigation is mounted in vacuum, on the cold finger of a liquid Helium continuous flow cryostat with a temperature range between 4.2 and 300 K. The microscope has a spatial resolution of 500 nm, the illumination is a monochromatic LED with a wavelength of 532 nm, and the maximum field of view is ~500×500 μm. The electric transport properties were measured in a two-probe configuration. For $NdNiO_3$, we used a Keithley 2400 SourceMeter configured as a current source, whereas we used a highly stable self-built current source for $SmNiO_3$.

Image Processing: For $NdNiO_3$, the gray values were normalized to a $NdNiO_3$ area that is not influenced by the resistive switching (not between the electrodes). For $SmNiO_3$, all the images are differential—the image with zero bias current is subtracted for each current.

A cryogenic s-SNOM system (cryo-neaSNOM from neaspec/attocube GmbH) was used for nanoscopic imaging of the filaments in the devices. Infrared radiation from a Quantum Cascade Laser (Daylight Solutions) was focused at a metal-coated AFM tip (ARROW-NCPt-50 from NanoAndMore GmbH), which was grounded to reduce the electrostatic interaction between the tip and the sample. Despite that, we had to avoid applying voltages >10 V in the microdevices, as it would disturb the AFM in tapping mode. The tip size determines the spatial resolution (20 nm in this case). Pseudoheterodyne detection allows separating far-field and near-field contributions to the signal by using higher-order tapping harmonics (the ratio between the intensity of the third and second harmonics is used in this paper). The detected near-field signal has an excellent spatial contrast between the insulating and metallic phases because of the large change of the optical

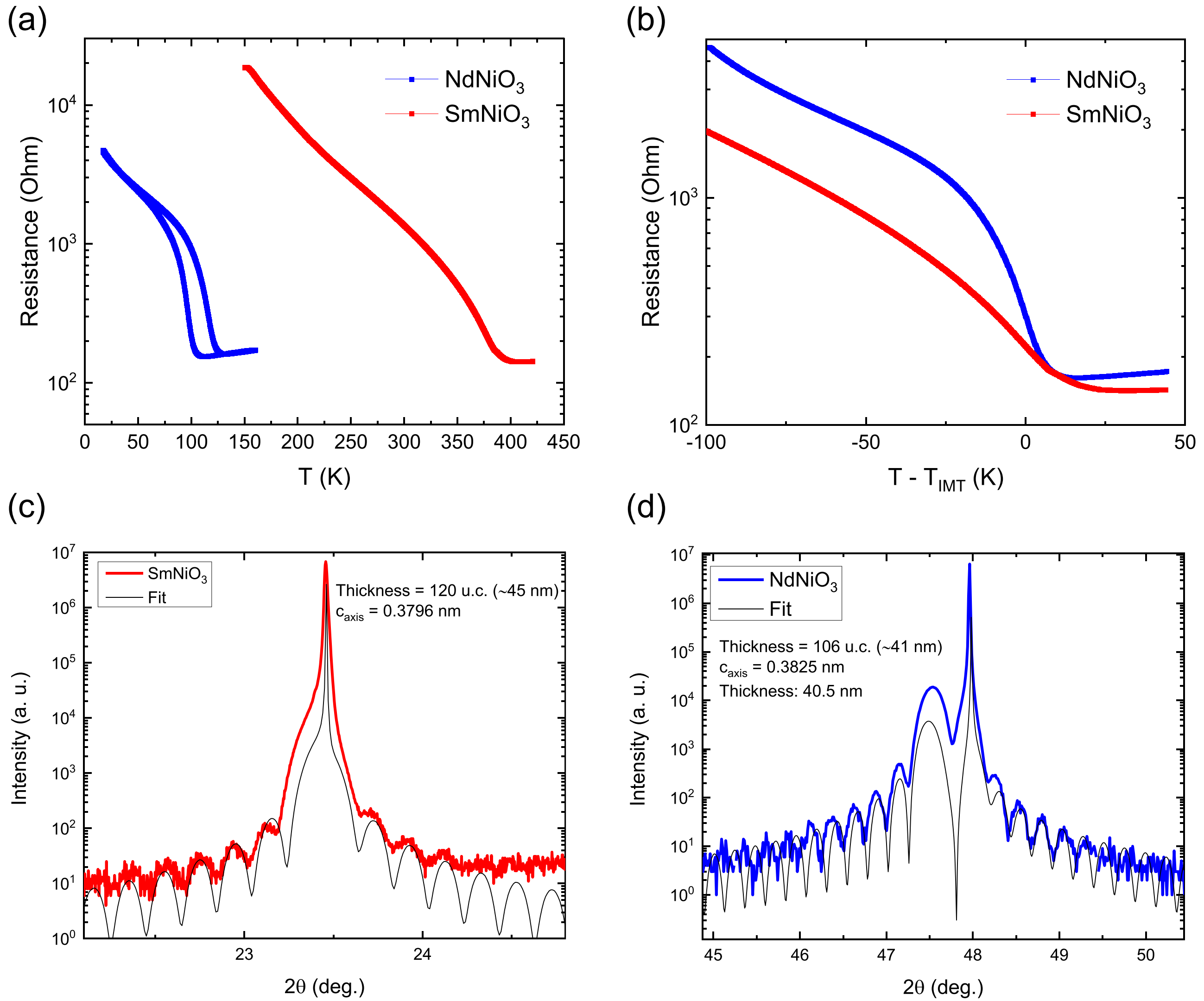

FIG. 6. Structural and transport properties of nickelate films and microdevices. (a) Two-probe resistance vs temperature characteristics of $NdNiO_3$ and $SmNiO_3$ microdevices, respectively. (b) Two-probe resistance plotted as a function of T-T_{IMT}. T_{IMT} was calculated finding the maximum of $\partial \log(\rho)/\partial T$, where ρ is the resistivity. Only the warmup branch is shown. $NdNiO_3$ shows a much sharper insulator-to-metal transition (IMT). (c) and (d) θ-2θ scans of the $SmNiO_3$ and $NdNiO_3$ films, respectively. Scans were performed around the (001) $LaAlO_3$ peak. Finite-sized oscillations are very visible, allowing us to determine the film thickness. Data were manually fitted using the InteractiveXRDfit software [43] and is shown in the plots as continuous dark lines. X-ray diffraction (XRD) shows high-quality epitaxial films with thicknesses ~40–45 nm.

conductivity across the IMT. More information about the s-SNOM operation can be found in Ref. [44].

APPENDIX C: RESISTOR NETWORK SIMULATIONS DETAILS

In the simulations presented in this paper, we use a phenomenological mesoscopic model known as the Mott Resistors Network [19,45]. The model describes the material as a matrix of cells, each containing four resistors, which connect the cell to its four nearest neighbors. Each cell corresponds to a small region of the material of the order of 10 nm. This scale is chosen to define a phase for the cell, which can be insulating or metallic. At first, all the resistors are initialized to a high insulating value, and all the cells are in the insulator phase. A voltage is applied to the mesh through the metallic electrodes that are situated at the top and the bottom, and currents begin to circulate in the resistor network. These currents can be computed, knowing the initial resistance and the applied voltage, using Kirchhoff laws. When the current I flows through the resistors R_{ij}, these generate heat according to Joule's law, with power $P = I^2R$. The heat generated by a cell is given by the sum of the contributions of its four resistors:

$$P_{ij}(t) = \left[I_1^2(t) + I_2^2(t) + I_3^2(t) + I_4^2(t)\right]R_{ij}(t),$$

where t indicates time in units of the simulation time step, ij are the indexes which identify the cell, P_{ij} is the power generated by the cell, R_{ij} is the resistance of the four resistors (which are always assumed to share the same value), and $I_1, I_2, I_3,$ and I_4 are the four currents flowing through them. Setting to unity the geometrical dimension of the cell, we can

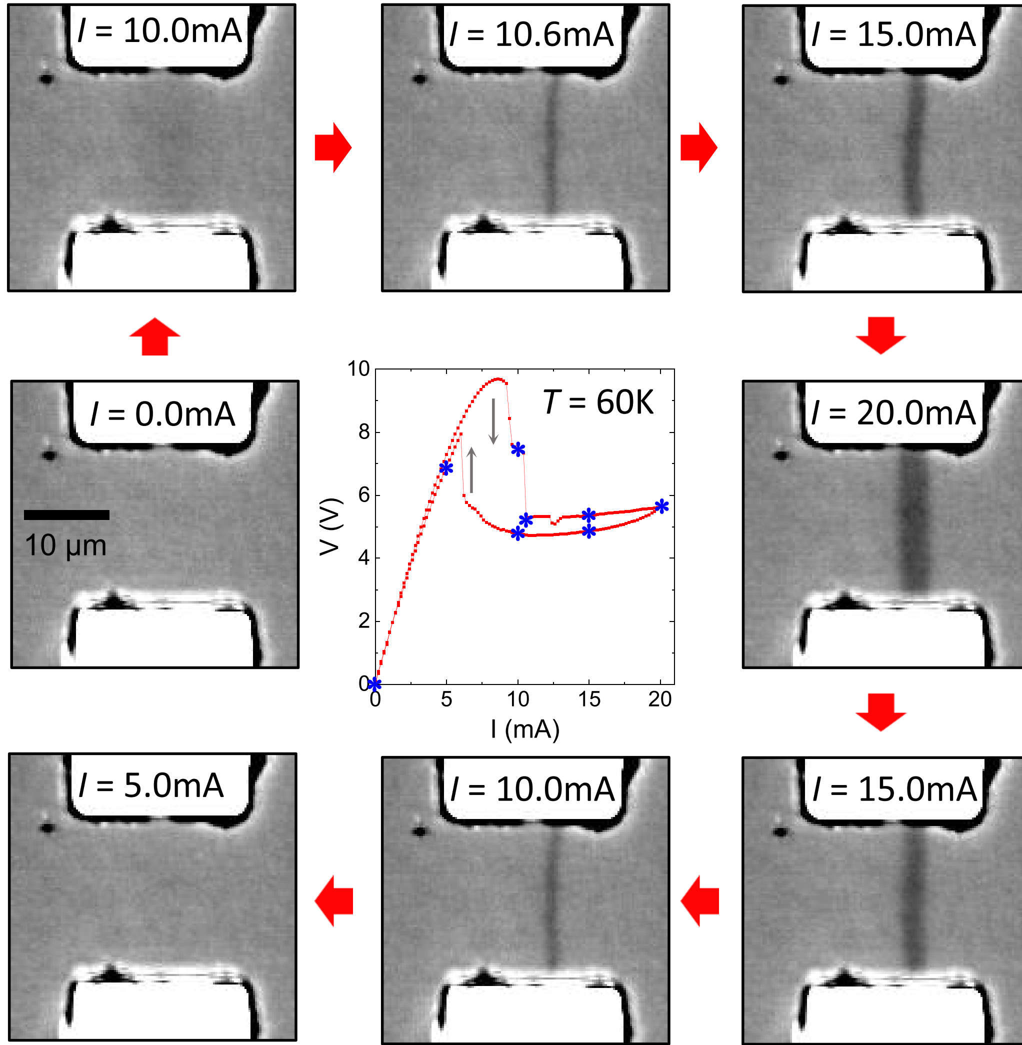

FIG. 7. Filament size dependence on applied current. Central panel: V-I characteristics of a $NdNiO_3$ microdevice at $T = 60$ K. Blue asterisks mark currents at which the outer panels where captured. Outer panels: Standard optical microscope images of the devices at different applied currents.

identify the resistivity of the cell with R_{ij}. The temperature of the cell will be the result of two contributions: Joule heating and a dissipative term that includes the dissipation to the nearest-neighbor cells and the dissipation to a substrate at a fixed temperature T_0, with which all the cells are in contact. Therefore, using the heat transfer equation, we can write the temperature of the cell as follows:

$$T_{ij}(t) = T_{ij}(t-1) + \frac{P_{ij}(t)}{C} - \frac{K}{C}\left[5T_{ij}(t-1) - \sum_{kl}^{NN} T_{kl}(t-1) - T_0\right],$$

where K is the thermal conductivity, C the thermal capacity, and the sum with indexes kl runs over the nearest-neighbor cells. We note that we have made the nonessential assumption of choosing the same thermal conductivity for the dissipation to the substrate and to the nearest neighbors and that the time step of the simulation Δt is set to unity.

The first-order transition of a cell from the insulator-to-metal phase (and vice versa) is described as a thermally activated behavior with a probability that depends on the temperature of the cell according to the following Arrhenius-like law:

$$p_{ij}^{a\to b}(t) = \exp\left[\frac{-E_B^{a\to b}(T_{ij})}{T_{ij}(t)}\right],$$

where a and b are the states of cell (insulator or metal), and E_B is the energy barrier that separates the two corresponding local minima as described by the following Landau-type free energy (which is appropriate for a first-order thermally driven transition):

$$f(\eta) = h\eta + p\eta^2 + c\eta^4,$$

$$h = h_1\frac{T - T_C}{T_C} + h_2,$$

$$p = p_1\frac{T - T_C}{T_C} + p_2.$$

Here, η is the order parameter, and T_C, h_1, h_2, p_1, and p_2 are constants. The resistivity of the cell is then chosen according

to the state of the cell: low and constant (ρ_{met}) in the metal state and high and temperature dependent in the insulator state [$\rho_{\text{ins}}(T)$]. We choose Mott's equation for variable range hopping [46] to describe the temperature dependence of the resistivity in the insulating state since it has already been used to fit the resistivity of $NdNiO_3$ samples [47,48]:

$$\rho_{\text{ins}}(T) = \rho_0 \exp\left[\Delta\left(\frac{1}{T} - \frac{1}{T_{\text{IMT}}}\right)^{1/4}\right],$$

where Δ is a constant, T_{IMT} is the metal-insulator transition temperature, and $\rho_0 = \rho(T_{\text{IMT}})$ is the resistivity at the transition temperature. Nevertheless, the specific choice of the functional form does not change the main qualitative features of the results. Once the resistivity of the cell has been computed, we can update the resistance of the resistors within it. When all the cells have been updated, the time step is increased by one, and the simulation continues as described above, starting again from the computation of Kirchhoff currents.

APPENDIX D: FILAMENT WIDTH DEPENDENCE ON CURRENT

Apart from temperature and specific material choice (the focus of this paper), filament size depends strongly on the applied current. This is a well-known effect [14–18] (see Supplemental Material [40]). A specific example is given in Fig. 7, which shows images of a $NdNiO_3$ microdevice at different points of a V-I measurement cycle, for a temperature $T =$ 60 K. As can be seen, the filament width grows with applied current, appearing and disappearing at the discontinuities of the ramp-up and ramp-down V-I curves, respectively.

APPENDIX E: DEVICE SELF-OSCILLATIONS

Interpretation of filament size is not straightforward for all currents. As can be seen in Figs. 2(a) and 2(d), for some temperatures, there are two voltage discontinuities when current is ramped up (for instance, at $T = 50$ K in $NdNiO_3$). Between the two, there is a range of currents where the V-I curve

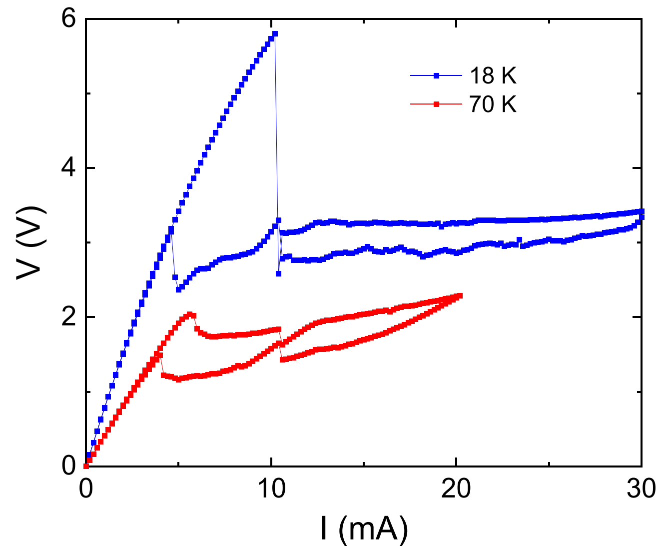

FIG. 8. Voltage vs current in $NdNiO_3$ microdevices, measured in the scattering-type scanning near-field optical microscopy (s-SNOM) setup. The characteristic features caused by device self-oscillation are absent.

is smooth and monotonically decreasing. In that range, the system is not stationary but rather oscillates between two configurations, one with a percolating filament and one without it. These self-oscillations, which are in the 10 kHz range, are a well-known effect [20,49], and they can be observed with an oscilloscope. The parasitic capacitance and the slow reaction time of current source are the main factors determining the oscillation regime. We must note that devices measured in the SNOM setup do not show the V-I characteristics associated with self-oscillations (Fig. 8). This difference is likely due to two main factors: (i) the different device geometry and (ii) the different wiring and parasitic capacitance of both setups.

All the analysis about filament size at different temperatures and materials shown in the paper is done for $I = 20$ mA. This is well above the self-oscillation range, where the system is stationary again, so it does not affect our conclusions.

[1] F. J. Morin, Oxides which Show a Metal-to-Insulator Transition at the Neel Temperature, Phys. Rev. Lett. **3**, 34 (1959).

[2] J. B. Torrance, P. Lacorre, A. I. Nazzal, E. J. Ansaldo, and C. Niedermayer, Systematic study of insulator-metal transitions in perovskites RNiO$_3$ (R = Pr, Nd, Sm, Eu) due to closing of charge-transfer gap, Phys. Rev. B **45**, 8209 (1992).

[3] M. Imada, A. Fujimori, and Y. Tokura, Metal-insulator transitions, Rev. Mod. Phys. **70**, 1039 (1998).

[4] S. Lupi, L. Baldassarre, B. Mansart, A. Perucchi, A. Barinov, P. Dudin, E. Papalazarou, F. Rodolakis, J. P. Rueff, J. P. Itié *et al.*, A microscopic view on the Mott transition in chromium-doped V_2O_3, Nat. Commun. **1**, 105 (2010).

[5] J. H. Park, J. M. Coy, T. Serkan Kasirga, C. Huang, Z. Fei, S. Hunter, and D. H. Cobden, Measurement of a solid-state triple point at the metal–insulator transition in VO_2, Nature (London) **500**, 431 (2013).

[6] S. Catalano, M. Gibert, J. Fowlie, J. Iñiguez, J. M. Triscone, and J. Kreisel, Rare-earth nickelates RNiO$_3$: Thin films and heterostructures, Rep. Prog. Phys. **81**, 046501 (2018).

[7] G. Stefanovich, A. Pergament, and D. Stefanovich, Electrical switching and Mott transition in VO_2, J. Phys. Condens. Matter **12**, 8837 (2000).

[8] G. Seo, B. J. Kim, C. Ko, Y. Cui, Y. W. Lee, J. H. Shin, S. Ramanathan, and H. T. Kim, Voltage-pulse-induced switching dynamics in VO_2, IEEE Electron Device Lett. **32**, 1582 (2011).

[9] P. Diener, E. Janod, B. Corraze, M. Querré, C. Adda, M. Guilloux-Viry, S. Cordier, A. Camjayi, M. Rozenberg, M. P. Besland *et al.*, How a dc Electric Field Drives Mott Insulators Out of Equilibrium, Phys. Rev. Lett. **121**, 016601 (2018).

[10] J. del Valle, N. M. Vargas, R. Rocco, P. Salev, Y. Kalcheim, P. N. Lapa, C. Adda, M.-H. Lee, P. Y. Wang, L. Fratino *et al.*,

Spatiotemporal characterization of the field-induced insulator-to-metal transition, Science **373**, 907 (2021).

[11] J. Del Valle, R. Rocco, C. Domínguez, J. Fowlie, S. Gariglio, M. J. Rozenberg, and J. M. Triscone, Dynamics of the electrically induced insulator-to-metal transition in rare-earth nickelates, Phys. Rev. B **104**, 165141 (2021).

[12] S. K. Das, S. Kumar Nandi, C. Verbel Marquez, A. Rúa, M. Uenuma, E. Puyoo, S. K. Nath, D. Albertini, N. Baboux, T. Lu *et al.*, Physical origin of negative differential resistance in V_3O_5 and its application as a solid-state oscillator, Adv. Mater. 2208477 (2022).

[13] A. Zimmers, L. Aigouy, M. Mortier, A. Sharoni, S. Wang, K. G. West, J. G. Ramirez, and I. K. Schuller, Role of Thermal Heating on the Voltage Induced Insulator-Metal Transition in VO_2, Phys. Rev. Lett. **110**, 056601 (2013).

[14] S. Kumar, M. D. Pickett, J. P. Strachan, G. Gibson, Y. Nishi, and R. S. Williams, Local temperature redistribution and structural transition during joule-heating-driven conductance switching in VO_2, Adv. Mater. **25**, 6128 (2013).

[15] S. Guénon, S. Scharinger, S. Wang, J. G. Ramírez, D. Koelle, R. Kleiner, and I. K. Schuller, Electrical breakdown in a V_2O_3 device at the insulator-to-metal transition, Europhys. Lett. **101**, 57003 (2013).

[16] H. Madan, M. Jerry, A. Pogrebnyakov, T. Mayer, and S. Datta, Quantitative mapping of phase coexistence in Mott-Peierls insulator during electronic and thermally driven phase transition, ACS Nano **9**, 2009 (2015).

[17] S. Kumar and R. S. Williams, Separation of current density and electric field domains caused by nonlinear electronic instabilities, Nat. Commun. **9**, 2030 (2018).

[18] M. Lange, S. Guénon, Y. Kalcheim, T. Luibrand, N. M. Vargas, D. Schwebius, R. Kleiner, I. K. Schuller, and D. Koelle, Imaging of Electrothermal Filament Formation in a Mott Insulator, Phys. Rev. Appl. **16**, 054027 (2021).

[19] R. Rocco, J. Del Valle, H. Navarro, P. Salev, I. K. Schuller, and M. Rozenberg, Exponential Escape Rate of Filamentary Incubation in Mott Spiking Neurons, Phys. Rev. Appl. **17**, 024028 (2022).

[20] C. Adda, M.-H. Lee, Y. Kalcheim, P. Salev, R. Rocco, N. M. Vargas, N. Ghazikhanian, C.-P. Li, G. Albright, M. Rozenberg *et al.*, Direct Observation of the Electrically Triggered Insulator-Metal Transition in V_3O_5 far below the Transition Temperature, Phys. Rev. X **12**, 011025 (2022).

[21] J. J. Yang, D. B. Strukov, and D. R. Stewart, Memristive devices for computing, Nat. Nanotechnol. **8**, 13 (2013).

[22] J. del Valle, P. Salev, F. Tesler, N. M. Vargas, Y. Kalcheim, P. Wang, J. Trastoy, M. H. Lee, G. Kassabian, J. G. Ramírez *et al.*, Subthreshold firing in Mott nanodevices, Nature (London) **569**, 388 (2019).

[23] M. D. Pickett, G. Medeiros-Ribeiro, and R. S. Williams, A scalable neuristor built with Mott memristors, Nat. Mater. **12**, 114 (2013).

[24] M. Ignatov, M. Ziegler, M. Hansen, A. Petraru, and H. Kohlstedt, A memristive spiking neuron with firing rate coding, Front. Neurosci. **9**, 376 (2015).

[25] P. Stoliar, J. Tranchant, B. Corraze, E. Janod, M.-P. P. Besland, F. Tesler, M. Rozenberg, and L. Cario, A leaky-integrate-and-fire neuron analog realized with a Mott insulator, Adv. Funct. Mater. **27**, 1604740 (2017).

[26] J. del Valle, P. Salev, Y. Kalcheim, and I. K. Schuller, A caloritronics-based Mott neuristor, Sci. Rep. **10**, 4292 (2020).

[27] W. Yi, K. K. Tsang, S. K. Lam, X. Bai, J. A. Crowell, and E. A. Flores, Biological plausibility and stochasticity in scalable VO_2 active memristor neurons, Nat. Commun. **9**, 4661 (2018).

[28] S. M. Bohaichuk, S. Kumar, G. Pitner, C. J. McClellan, J. Jeong, M. G. Samant, H. S. P. Wong, S. S. P. Parkin, R. S. Williams, and E. Pop, Fast spiking of a Mott VO_2–carbon nanotube composite device, Nano Lett. **19**, 6751 (2019).

[29] S. Oh, Y. Shi, J. del Valle, P. Salev, Y. Lu, Z. Huang, Y. Kalcheim, I. K. Schuller, and D. Kuzum, Energy-efficient Mott activation neuron for full-hardware implementation of neural networks, Nat. Nanotechnol. **16**, 680 (2021).

[30] S. Kumar, J. P. Strachan, and R. S. Williams, Chaotic dynamics in nanoscale NbO_2 Mott memristors for analogue computing, Nature (London) **548**, 318 (2017).

[31] M. Jerry, K. Ni, A. Parihar, A. Raychowdhury, and S. Datta, Stochastic insulator-to-metal phase transition-based true random number generator, IEEE Electron Device Lett. **39**, 139 (2018).

[32] J. del Valle, P. Salev, S. Gariglio, Y. Kalcheim, I. K. Schuller, and J.-M. Triscone, Generation of tunable stochastic sequences using the insulator–metal transition, Nano Lett. **22**, 1251 (2022).

[33] S. Cueff, J. John, Z. Zhang, J. Parra, J. Sun, R. Orobtchouk, S. Ramanathan, and P. Sanchis, VO_2 nanophotonics, APL Photonics **5**, 110901 (2020).

[34] G. Li, D. Xie, H. Zhong, Z. Zhang, X. Fu, Q. Zhou, Q. Li, H. Ni, J. Wang, E. jia Guo *et al.*, Photo-induced non-volatile VO_2 phase transition for neuromorphic ultraviolet sensors, Nat. Commun. **13**, 1729 (2022).

[35] I. Olivares, J.-P. Locquet, J. Parra, L. D. Sánchez, M. Menghini, P. Sanchis, and P. Homm, Experimental demonstration of a tunable transverse electric pass polarizer based on hybrid VO_2/silicon technology, Opt. Lett. **43**, 3650 (2018).

[36] K. J. Miller, K. A. Hallman, R. F. Haglund Jr, and S. M. Weiss, Silicon waveguide optical switch with embedded phase change material, Opt. Express **25**, 26527 (2017).

[37] D. Lee, J. Lee, K. Song, F. Xue, S. Y. Choi, Y. Ma, J. Podkaminer, D. Liu, S. C. Liu, B. Chung *et al.*, Sharpened VO_2 phase transition via controlled release of epitaxial strain, Nano Lett. **17**, 5614 (2017).

[38] M. Lange, S. Guénon, F. Lever, R. Kleiner, and D. Koelle, A high-resolution combined scanning laser and widefield polarizing microscope for imaging at temperatures from 4 K to 300 K, Rev. Sci. Instrum. **88**, 123705 (2017).

[39] K. W. Post, A. S. McLeod, M. Hepting, M. Bluschke, Y. Wang, G. Cristiani, G. Logvenov, A. Charnukha, G. X. Ni, P. Radhakrishnan *et al.*, Coexisting first- and second-order electronic phase transitions in a correlated oxide, Nat. Phys. **14**, 1056 (2018).

[40] See Supplemental Material at http://link.aps.org/supplemental/10.1103/PhysRevResearch.5.013108 for videos showing the current dependence at different temperatures.

[41] E. Sediva, W. J. Bowman, J. C. Gonzalez-Rosillo, and J. L. M. Rupp, Investigation of the eightwise switching mechanism and its suppression in $SrTiO_3$ modulated by humidity and interchanged top and bottom platinum and $LaNiO_3$ electrode contacts, Adv. Electron. Mater. **5**, 1800566 (2018).

[42] W. Schnelle, R. Fischer, and E. Gmelin, Specific heat capacity and thermal conductivity of $NdGaO_3$ and $LaAlO_3$ single crystals at low temperatures, J. Phys. D: Appl. Phys. **34**, 846 (2001).

[43] C. Lichtensteiger, InteractiveXRDFit: A new tool to simulate and fit X-ray diffractograms of oxide thin films and heterostructures, J. Appl. Crystallogr. **51**, 1745 (2018).

[44] X. Chen, D. Hu, R. Mescall, G. You, D. N. Basov, Q. Dai, and Mengkun Liu, Modern scattering-type scanning near-field optical microscopy for advanced material research, Adv. Mater. **31**, 1804774 (2019).

[45] P. Stoliar, L. Cario, E. Janod, B. Corraze, C. Guillot-Deudon, S. Salmon-Bourmand, V. Guiot, J. Tranchant, and M. Rozenberg, Universal electric-field-driven resistive transition in narrow-gap Mott insulators, Adv. Mater. **25**, 3222 (2013).

[46] N. F. Mott, *Metal-Insulator Transitions* (Taylor & Francis, London, 1990).

[47] J. Blasco, M. Castro, and J. Garcia, Structural, electronic, magnetic and calorimetric study of the metal-insulator transition in $NdNiO_{3-\delta}$, J. Phys.: Condens. Matter **6**, 5875 (1994).

[48] G. Catalan, R. M. Bowman, and J. M. Gregg, Metal-insulator transitions in $NdNiO_3$ thin films, Phys. Rev. B **62**, 7892 (2000).

[49] Y. W. Lee, B.-J. Kim, J.-W. Lim, S. J. Yun, S. Choi, B.-G. Chae, G. Kim, and H.-T. Kim, Metal-insulator transition-induced electrical oscillation in vanadium dioxide thin film, Appl. Phys. Lett. **92**, 162903 (2008).